Noncentrosymmetric characteristics of defects on WTe_2

Wan-Hsin Chen,[1,4] Naoya Kawakami,[1,4] Jhe-Jhih Lin,[1,4] Hsiang-I Huang,[1,4] Ryuichi Arafune,[2] Noriaki Takagi,[3] and Chun-Liang Lin[1,4]

[1]*Department of Electrophysics, National Yang Ming Chiao Tung University, 1001 University Road, Hsinchu 300, Taiwan*
[2]*International Center for Materials Nanoarchitectonics, National Institute for Materials Science, 1-1 Namiki, Ibaraki 304-0044, Japan*
[3]*Graduate School of Human and Environmental Studies, Kyoto University, Kyoto 606-8501, Japan*
[4]*Department of Electrophysics, National Chiao Tung University, 1001 University Road, Hsinchu 300, Taiwan*

(Received 12 March 2021; accepted 8 August 2022; published 26 August 2022)

Tungsten ditelluride (WTe_2) is a transition metal dichalcogenide with novel electronic structures and unique properties for application to next-generation devices. Defects in WTe_2 can impact its properties in both positive and negative ways. Therefore, it urgently requires a precise classification to help understand the possible impacts. Here we report on both geometric and electronic characteristics of the defects in WTe_2 identified by the combination of scanning tunneling microscopy (STM) and density functional theory (DFT) calculation. We found four types of defects derived from a missing Te atom; two of them are located at the topmost surface while the others are under the surface. The former are imaged topographically and are ascribed to point vacancies of surface Te atoms. The DFT calculations reveal the noncentrosymmetric displacements of atoms around the defects and reasonably reproduce the STM images. Interestingly, the latter defects are hardly observed but they are dressed with the noncentrosymmetric quasiparticle interference (QPI) fringes which enable us to identify them. These findings demonstrate that STM-QPI can be a feasible method to characterize the defects in layered materials.

DOI: 10.1103/PhysRevB.106.075428

I. INTRODUCTION

Layered materials stacked up by van der Waals interaction have gathered a lot of attention in more than a decade because of their intriguing properties and extremely high potential in electronics, optoelectronics, spintronics, and energy conversion and storage. Among layered materials, transition metal dichalcogenides (TMDs) occupy a significant share with the variable combination of MX_2, where M is a transition metal atom and X is a chalcogen atom. More than graphene, TMDs exhibit diverse properties such as tunable band gaps and light-emitting and unconventional superconductivity [1–5].

Tungsten ditelluride (WTe_2), a unique material of the TMD family, has the T_d-phase structure in its natural ground state and exhibits almost the largest spin-orbital coupling among all TMDs [6]. Several exotic properties in WTe_2 have been reported such as extremely large nonsaturating magnetoresistance up to 60 T [7], pressure-induced superconductivity [8,9], and a Lifshitz transition in Fermi surface topology [10]. WTe_2 has also been predicted to be a type-II Weyl semimetal [11], which boosts the competition to reveal the topological features by using angle-resolved photoemission spectroscopy [12–17] and scanning tunneling microscopy (STM) [18–22]. Lin *et al.* measured quasiparticle interference (QPI) by using STM to visualize the Weyl points and Fermi arc surface states [18]. In addition, the few-layer WTe_2 shows spontaneous out-of-plane electric polarization [23] and the surface dipole strongly depends on the thickness [24].

Atomic-scale defects inevitably appear in TMDs even when they are grown by molecular beam epitaxy [25]. It is widely agreed that defects will greatly affect the electronic, magnetic, transport, and optical properties of TMDs [26–30], which play a key role in generating unexpected features. However, our understanding of defects in WTe_2 is not yet comprehensive. Early STM studies [31,32] were made for WTe_2 cleaved in air and loaded into ultrahigh vacuum (UHV), and reported the point defects which are tentatively ascribed to vacancies of surface Te atoms. Recent STM studies [18–22] also report the defects, but these studies mainly focus on the electronic structure relevant to Weyl semimetal so that the details about the defects are not thoroughly scrutinized. A density functional theory (DFT) study [33] has been performed for the vacancies of Te or W atoms, but the comparison is not conducted between simulated and experimentally observed STM images. Besides, the Te vacancies impact the properties of semimetals. The Te vacancies in $MoTe_2$ make $1T'$- and T_d-$MoTe_2$ become more metallic [34]. Moreover, a very recent DFT calculation shows that Te vacancies in monolayer WTe_2 strongly influence the band structure and the topological property is destroyed at the nominal composition of $WTe_{1.97}$ [35]. The defects in WTe_2 still remain to be explored.

In this study, we used STM and DFT calculations to identify the defects in WTe_2. We found four types of point vacancies formed by removing a Te atom on the topmost surface and under the surface. These vacancies generate the distinctive QPI fringes reflecting the noncentrosymmetric crystal structure to identify them even when they are hardly imaged topographically. These results indicate that STM-QPI is a significant way to identify the defects.

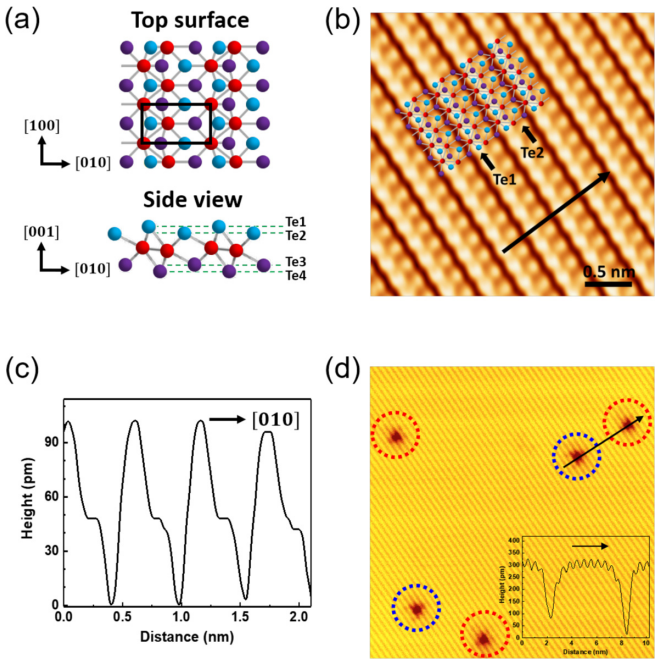

FIG. 1. (a) Atomic model of T_d-WTe_2. (b) High resolution STM image overlapped with the atomic model ($V = 178\,\text{mV}, I = 0.7\,\text{nA}$). (c) Line profile along the arrow in (b). (d) Topographic STM image of *in situ* cleaved WTe_2 surface ($V = -473\,\text{mV}, I = 0.8\,\text{nA}$). The image size is $28 \times 28\,\text{nm}^2$. The inset shows the line profile across the two different defects.

II. METHODS

All the experiments were carried out in a UHV chamber. The base pressure was kept under 2×10^{-10} torr. We used high-quality T_d-WTe_2 crystals from HQ Graphene Company, The Netherlands. The crystal structure was once examined by low-energy electron diffraction [36]. The STM images were acquired at 5 K after *in situ* cleaving. dI/dV mapping was obtained by a lock-in technique with modulation of 10 mV at the frequency from 400 to 800 Hz.

All the DFT calculations were carried out using the Vienna Ab Initio Simulation Package (VASP) [37,38] with the projected augmented wave (PAW) method [39]. The exchange and correlation functional was described at the level of a generalized gradient approximation (GGA) parametrized by Perdew *et al.* [40]. The cutoff energy of the plane wave expansion used was 400 eV. To model the isolated defect in the surface WTe_2 layer, we used a 9×9 supercell of bilayer T_d-WTe_2 (648 W and 1296 Te atoms were used to represent the defect-free WTe_2 slab). A dipole correction and the spin-orbit coupling were taken into account. The Brillouin zone was sampled at the Γ point alone because of the large dimension of the supercell. The atoms in the top three layers were optimized without any constraint until the force on individual atoms was less than $0.02\,\text{eV Å}^{-1}$.

III. RESULTS

Bulk T_d-WTe_2 crystal takes a layered structure in which WTe_2 layers are piled up. Each WTe_2 layer consists of three atomic layers as shown in Fig. 1(a). The top and bottom layers are composed of nonequivalent Te atoms while the middle layer consists of W atoms. Hereafter, we denote the nonequivalent Te atoms in the top (bottom) layer as Te1 and Te2 (Te3 and Te4), respectively. The Te1 (Te4) atoms in the top (bottom) layer are located at the outer side with respect to the Te2 (Te3) atoms. Cleavage of bulk crystal leads to a Te-terminated (001) surface as depicted in Fig. 1(a).

Figure 1(b) shows an atomic resolution STM image of the WTe_2 surface after *in situ* cleaving. A pair of atomic rows are aligned and the brighter ones are separated by 0.63 nm along the black arrow as the height profile in Fig. 1(c) shows. Thus, the brighter rows are relevant to Te1 atoms and the other rows consist of the Te2 atoms. The surface structure in Fig. 1(b) well matches the superimposed atomic structure. Additionally, two Te atomic rows can be confirmed by bias-dependent measurement; see Supplemental Material Fig. S1 [41]. Figure 1(d) shows an image of a wider area. Bright stripes and two types of dark depressions are observed which are marked by red and blue circles, respectively. The depressions are the defects. The line profiles across the two different defects are shown in the inset of Fig. 1(d). Since the formation energy of a single chalcogen element defect is the lowest [42], we are more inclined to see the defect as a chalcogen vacancy.

Figures 2(a) and 2(b) show the two types of defects observed in Fig. 1(d). The defects appear as dark spots in the images. The spot in Fig. 2(a) locates in the atomic row of the Te1 atoms, while that in Fig. 2(b) is in the row of the Te2 atoms. The size of each spot is comparable with that of a single Te atom. These features indicate that the defect in Fig. 2(a) [Fig. 2(b)] is ascribed to a vacancy of a Te1 (Te2) atom. Here we call these vacancies V-Te1 and V-Te2, respectively.

Taking a look at the local contrasts around V-Te1 and V-Te2 in the topographic images, both sides of V-Te1 are symmetrically bright with respect to the [010] direction (i.e., vertical direction) while the contrast looks horizontally asymmetrical. The lower part is slightly brighter than the upper part. The contrast around V-Te2 looks symmetrical with respect to the [010] direction and it slightly differs in between the upper and lower parts. In addition, the dark hole can be understood by overlapping the topographic images with the corresponding atomic models (see Supplemental Material Fig. S2 [41]).

The DFT calculations support that the defects are derived from the vacancies of Te1 and Te2 atoms. (A more comprehensive categorization and discussion can be found in Supplemental Material Fig. S3.) The simulated STM images for both V-Te1 and V-Te2 are shown in Figs. 2(c) and 2(d) together with the atomic models in Figs. 2(e) and 2(f), respectively. The symmetrical and asymmetrical features observed for both V-Te1 and V-Te2 are reasonably reproduced. Although some detailed features in the simulated images are difficult to be revealed by STM, the similarities in the main features lead us to conclude our assignments of defects. In Fig. 2(c), the Te atoms on both sides of V-Te1 are bright. This is matched with the local feature around V-Te1 in Fig. 2(a). The Te atoms at the upper side of V-Te2 are slightly brighter in Fig. 2(d), which basically reproduces the asymmetrical feature around V-Te2 in Fig. 2(b).

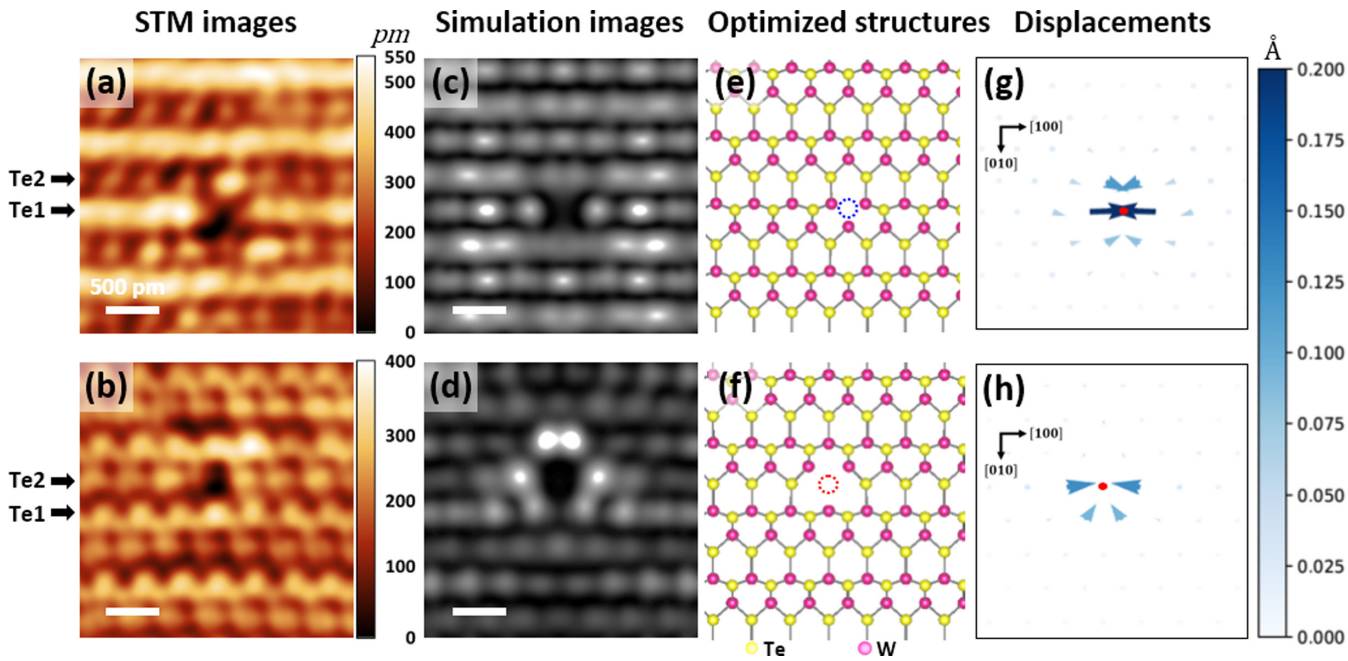

FIG. 2. Two types of Te vacancy defect. (a), (b) High resolution STM images acquired for two types of intrinsic defects on the topmost surface ($V = -122$ mV, $I = 0.76$ nA and $V = -127$ mV, $I = 0.91$ nA, respectively). (c), (d) Simulated STM images ($V = -50$ mV and $V = -50$ mV, respectively) of the defects in (a) and (b). (e), (f) Optimized atomic structures around the defects created by V-Te1 and V-Te2, respectively. (g), (h) The displacements of topmost Te atoms around the V-Te1 and V-Te2, respectively. All images are horizontally aligned. [010] and [100] directions can be found in both (g) and (h).

It is important to consider O substitution (i.e., a Te atom is replaced by an O atom) because they often can be found on the surface of TMD materials. From the simulated STM images, both V-Te2 and O-Te2 (O replaces Te2; see Supplemental Material Fig. S4) show similar symmetry and a dark hole in the center. However, a further experiment shows that O substitution defects appear only after exposure to O_2 (see Supplemental Material Fig. S5). Since we cleaved the sample in a UHV chamber, those two types of defects in Fig. 2 are strong candidates for Te vacancy, not O substitution. Note that the defect of O substitution also causes noncentrosymmetric characters to appear in the STM image, agreeing with the DFT simulation. The previous DFT study has calculated V-Te1 and V-Te2 [33]. The current results are consistent with the previous DFT results, which strengthens our assignments of V-Te1 and V-Te2.

Our DFT calculations also provide insights on the noncentrosymmetric features observed around V-Te1 and V-Te2. The atomic displacements around V-Te1 and V-Te2 are shown in Figs. 2(g) and 2(h), respectively. Each arrow represents the direction and the magnitude of the atomic displacement. The red dot is the position of the Te vacancy. The atomic displacements around V-Te1 and V-Te2 are mirror-symmetric with respect to the [010] direction, whereas these are asymmetrical with respect to the [100] direction. In the case of V-Te1, the displacements at the upper side are larger than those at the lower side; on the contrary, the displacements at the lower side are larger around V-Te2. These noncentrosymmetric displacements affect the electron distribution around both vacancies, leading to the noncentrosymmetric features around V-Te1 and V-Te2 in the STM images.

In general, the defects on the topmost surface can be easily imaged and identified by STM, whereas it is difficult to visualize the defects located below the surface. We performed dI/dV spectra measurements on the top defect, bottom defect, and defect-free surface to characterize the electronic structures (see Supplemental Material Fig. S6). However, due to the semimetal nature of the WTe_2, the difference of dI/dV spectra regarding three regions appears as neither specific states nor noticeable changes as those for semiconducting TMD materials [43]. On the contrary, the dI/dV mapping provides a solution as it has been applied to probe the defects and impurities under the surface [44,45]. Here, we have demonstrated that the defects under the surface can be identified through the QPI fringes due to the defects measured by the dI/dV mapping.

Figures 3(a) and 3(b) show the topographic and dI/dV mapping images of the same area simultaneously taken at $V = 200$ mV, respectively. In Fig. 3(a), V-Te1 and V-Te2 are observed as marked by blue and red circles, respectively. The QPI fringes caused by V-Te1 and V-Te2 are also observed in Fig. 3(b) as shown by blue and red circles. In addition to those fringes, other QPI fringes appear in Fig. 3(b) as highlighted by pink and green circles. Interestingly, topographic features corresponding to these fringes are hardly observed in Fig. 3(a). This implies that the defects other than V-Te1 and V-Te2 locate under the surface, giving rise to the QPI fringes. These fringes are also observed at different sample voltages as shown in Figs. 3(c)–3(f). The amplitudes are almost identical over the voltages. This voltage dependence is similar to that of the fringes derived from V-Te1 and V-Te2. The former indicates that the defects are likely in the same layer under

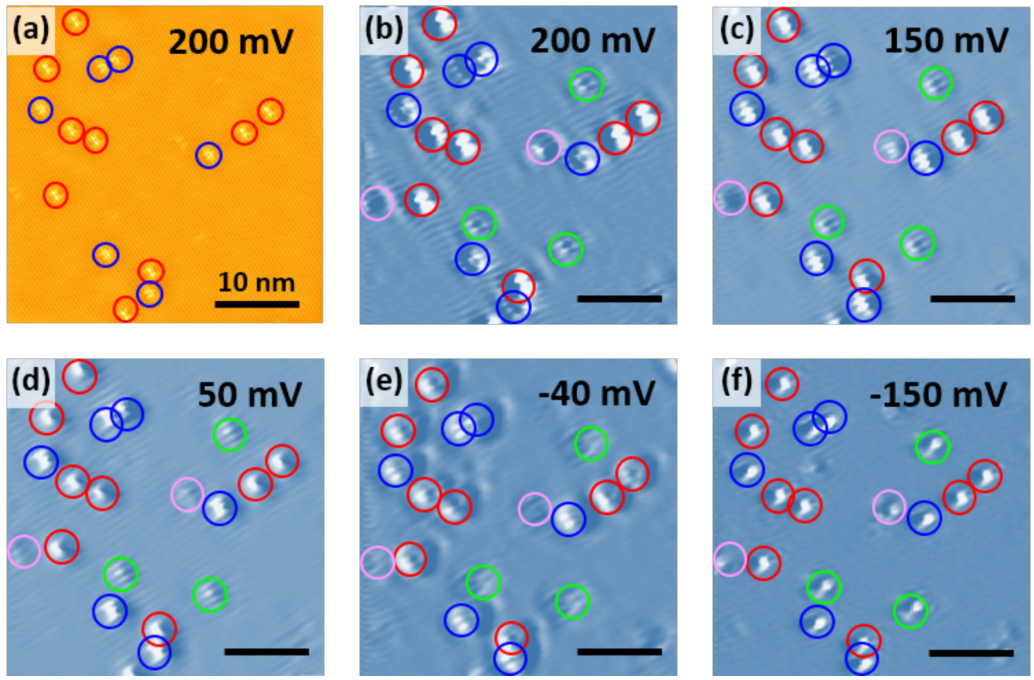

FIG. 3. WTe_2 surface with several defects revealed by (a) typical topographic image and dI/dV mapping at the same area with (b) 200 mV, (c) 150 mV, (d) 50 mV, (e) −40 mV, and (f) −150 mV. V-Te1 and V-Te2 are marked by red and blue circles. Additional two types of defects observed in the dI/dV mapping are marked by pink and green circles.

the surface and the latter implies that the types of the defects under the surface are similar to V-Te1 and V-Te2. Since the tungsten vacancies present a large noncentrosymmetric electronic depression on the surface, these defects are easier to observe than Te vacancies at the bottom layer (see Supplemental Material Fig. S2). In addition, chalcogen vacancies are the most common point defects in TMDs [46], and usually these defects can cause anisotropic and unique voltage-dependent QPI fringes nearby [45]. Thus, it is highly possible that the defects under the perfect surface are attributed to the point vacancies relevant to Te3 or Te4 atom in the bottom Te layer in the WTe_2 layer.

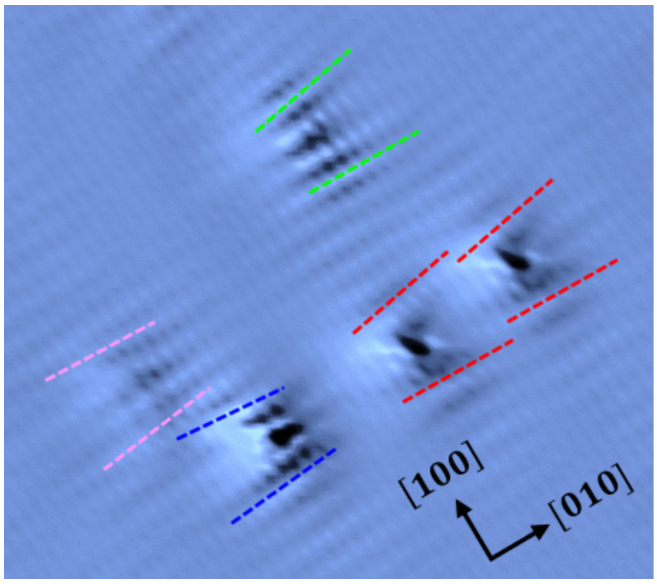

FIG. 4. Magnified image of WTe_2 surface with four types of fringe patterns revealed by dI/dV mapping ($25 \times 20\,nm^2$, $V = 160\,mV$). The antinodes of respective fringes are depicted by blue, red, green, and pink dashed lines for V-Te1, V-Te2, and vacancies under the surface, respectively.

The QPI fringes derived from the Te vacancies show characteristic asymmetricity which helps us distinguish them as a fingerprint. Figure 4(a) is a magnified image of dI/dV mapping. The fringes due to the four types of vacancies are classified by their symmetries. The antinodes of respective fringes are depicted by blue, red, green, and pink dashed lines for V-Te1, V-Te2, and vacancies under the surface, respectively. Each pair of lines are symmetric with respect to the [010] direction, and the lines are tilted relative to the [010] direction. The fringes of V-Te1 and V-Te2 show opposite asymmetries, i.e., they have parities. This reflects the symmetry difference in scattering potential between V-Te1 and V-Te2 and the noncentrosymmetric displacements of atoms around V-Te1 and V-Te2. This is true for the fringes of vacancies under the surface as depicted by green and pink lines. These fringes are classified by the similar parities. Considering that the vacancies of Te3 and Te4 in the bottom atomic layer are likely candidates for the defects, the parities of Te3 and Te4 vacancies should coincide with those of V-Te2 and V-Te1, respectively, because the atomic structures of top and bottom Te layers are inverted. Thus, we believe that the fringes marked by green and pink lines are assigned to be the point vacancies of Te4 and Te3 atoms.

IV. CONCLUSION

To conclude, we have investigated the structural and electronic properties of defects in WTe_2 through STM and DFT calculation. Four types of defects are found. Two of them are topographically imaged and the other two are hardly visible. The former are assigned to be point vacancies caused by missing a Te1 or Te2 atom on the topmost surface. The DFT calculations reveal that the displacements of atoms around these vacancies are noncentrosymmetric, leading to the asymmetrical features around these vacancies observed by STM. The latter defects are probed by measuring QPI fringes and we ascribe them to the vacancies of Te atoms under the surface. In addition, we found that the QPI fringes due to the vacancies are uniquely reflecting the noncentrosymmetric crystal structure and can be a fingerprint to specify them. We demonstrate that the combination of STM imaging and dI/dV mapping is a useful method to probe defects not only at the surface but also under the surface. Further explorations of defects with this method on other layered materials are highly expected.

ACKNOWLEDGMENTS

This work was financially supported by the "Center for the Semiconductor Technology Research" from The Featured Areas Research Center Program within the framework of the Higher Education Sprout Project by the Ministry of Education (MOE) in Taiwan. This work was also supported in part by the Ministry of Science and Technology, Taiwan, under Grants No. MOST 110-2634-F-009-027, No. 110-2112-M-A49-013-MY3, and No. MOST 110-2112-M-A49-022-MY2, and by the Ministry of Education, Culture, Sports, Science, and Technology (MEXT) through Grants-in-Aid for Scientific Research (No. 24241040, No. 25110008, No. 20K05326, and No. 22H01960).

[1] Q. H. Wang, K. Kalantar-Zadeh, A. Kis, J. N. Coleman, and M. S. Strano, Nat. Nanotechnol. **7**, 699 (2012).
[2] K. Novoselov, A. Mishchenko, A. Carvalho, and A. Castro Neto, Science **353**, aac9439 (2016).
[3] S. Manzeli, D. Ovchinnikov, D. Pasquier, O. Yazyev, and A. Kis, Nat. Rev. Mater. **2**, 17033 (2017).
[4] A. Eftekhari, J. Mater. Chem. A **5**, 18299 (2017).
[5] J. Shang, X. Shen, C. Cong, N. Peimyoo, B. Cao, M. Eginligil, and T. Yu, ACS Nano **9**, 647 (2015).
[6] X. Qian, J. Liu, L. Fu, and J. Li, Science **346**, 1344 (2014).
[7] M. N. Ali, J. Xiong, S. Flynn, J. Tao, Q. D. Gibson, L. M. Schoop, T. Liang, N. Haldolaarachchige, M. Hirschberger, N. P. Ong, and R. J. Cava, Nature (London) **514**, 205 (2014).
[8] D. Kang, Y. Zhou, W. Yi, C. Yang, J. Guo, Y. Shi, S. Zhang, Z. Wang, C. Zhang, S. Jiang, A. Li, K. Yang, Q. Wu, G. Zhang, L. Sun, and Z. Zhao, Nat. Commun. **6**, 7804 (2015).
[9] X. C. Pan, X. Chen, H. Liu, Y. Feng, Z. Wei, Y. Zhou, Z. Chi, L. Pi, F. Yen, F. Song, X. Wan, Z. Yang, B. Wang, G. Wang, and Y. Zhang, Nat. Commun. **6**, 7805 (2015).
[10] Y. Wu, N. H. Jo, M. Ochi, L. Huang, D. Mou, S. L. Bud'ko, P. C. Canfield, N. Trivedi, R. Arita, and A. Kaminski, Phys. Rev. Lett. **115**, 166602 (2015).
[11] A. Soluyanov, D. Gresch, Z. Wang, Q. Wu, M. Troyer, X. Dai, and B. Bernevig, Nature (London) **527**, 495 (2015).
[12] C. Wang, Y. Zhang, J. Huang, S. Nie, G. Liu, A. Liang, Y. Zhang, B. Shen, J. Liu, C. Hu, Y. Ding, D. Liu, Y. Hu, S. He, L. Zhao, L. Yu, J. Hu, J. Wei, Z. Mao, Y. Shi *et al.*, Phys. Rev. B **94**, 241119(R) (2016).
[13] F. Y. Bruno, A. Tamai, Q. S. Wu, I. Cucchi, C. Barreteau, A. de la Torre, S. McKeown Walker, S. Riccò, Z. Wang, T. K. Kim, M. Hoesch, M. Shi, N. C. Plumb, E. Giannini, A. A. Soluyanov, and F. Baumberger, Phys. Rev. B **94**, 121112(R) (2016).
[14] J. Sánchez-Barriga, M. G. Vergniory, D. Evtushinsky, I. Aguilera, A. Varykhalov, S. Blügel, and O. Rader, Phys. Rev. B **94**, 161401(R) (2016).
[15] J. Jiang, F. Tang, X. C. Pan, H. M. Liu, X. H. Niu, Y. X. Wang, D. F. Xu, H. F. Yang, B. P. Xie, F. Q. Song, P. Dudin, T. K. Kim, M. Hoesch, P. K. Das, I. Vobornik, X. G. Wan, and D. L. Feng, Phys. Rev. Lett. **115**, 166601 (2015).
[16] P. K. Das, D. D. Sante, I. Vobornik, J. Fujii, T. Okuda, E. Bruyer, A. Gyenis, B. E. Feldman, J. Tao, R. Ciancio, G. Rossi, M. N. Ali, S. Picozzi, A. Yadzani, G. Panaccione, and R. J. Cava, Nat. Commun. **7**, 10847 (2016).
[17] B. Feng, Y. H. Chan, Y. Feng, R. Y. Liu, M. Y. Chou, K. Kuroda, K. Yaji, A. Harasawa, P. Moras, A. Barinov, W. Malaeb, C. Bareille, T. Kondo, S. Shin, F. Komori, T. C. Chiang, Y. Shi, and I. Matsuda, Phys. Rev. B **94**, 195134 (2016).
[18] C. L. Lin, R. Arafune, R. Y. Liu, M. Yoshimura, B. Feng, K. Kawahara, Z. Ni, E. Minamitani, S. Watanabe, Y. Shi, M. Kawai, T. C. Chiang, I. Matsuda, and N. Takagi, ACS Nano **11**, 11459 (2017).
[19] W. Zhang, Q. Wu, L. Zhang, S. W. Cheong, A. A. Soluyanov, and W. Wu, Phys. Rev. B **96**, 165125 (2017).
[20] L. Peng, Y. Yuan, G. Li, X. Yang, J. J. Xian, C. J. Yi, Y. G. Shi, and Y. S. Fu, Nat. Commun. **8**, 659 (2017).
[21] Y. Yuan, X. Yang, L. Peng, Z. J. Wang, J. Li, C. J. Yi, J. J. Xian, Y. G. Shi, and Y. S. Fu, Phys. Rev. B **97**, 165435 (2018).
[22] P. Rüßmann, A. P. Weber, F. Glott, N. Xu, M. Fanciulli, S. Muff, A. Magrez, P. Bugnon, H. Berger, M. Bode, J. H. Dil, S. Blügel, P. Mavropoulos, and P. Sessi, Phys. Rev. B **97**, 075106 (2018).
[23] Z. Fei, W. Zhao, T. A. Palomaki, B. Sun, M. K. Miller, Z. Zhao, J. Yan, X. Xu, and D. H. Cobden, Nature (London) **560**, 336 (2018).
[24] Z. Ni, E. Minamitani, K. Kawahara, R. Arafune, C. L. Lin, N. Takagi, and S. Watanabe, J. Phys. Chem. C **124**, 2008 (2020).
[25] X. Zhao, P. Song, C. Wang, A. Riis-Jensen, W. Fu, Y. Deng, D. Wan, L. Kang, S. Ning, J. Dan, T. Venkatesan, Z. Liu, W. Zhou, K. S. Thygesen, X. Luo, S. J. Pennycook, and K. P. Loh, Nature (London) **581**, 171 (2020).
[26] M. Aghajanian, A. Mostofi, and J. Lischner, Sci. Rep. **8**, 13611 (2018).
[27] W. F. Li, C. Fang, and M. A. van Huis, Phys. Rev. B **94**, 195425 (2016).
[28] S. Barja, S. Refaely-Abramson, B. Schuler, D. Y. Qiu, A. Pulkin, S. Wickenburg, H. Ryu, M. M. Ugeda, C. Kastl, C. Chen, C. Hwang, A. Schwartzberg, S. Aloni, S. K. Mo, D. F. Ogletree, M. F. Crommie, O. V. Yazyev, S. G. Louie, J.

B. Neaton, and A. Weber-Bargioni, Nat. Commun. **10**, 3382 (2019).
[29] B. Schuler, J. Lee, C. Kastl, K. Cochrane, C. Chen, S. Refaely-Abramson, S. Yuan, E. van Veen, R. Roldán, N. Borys, R. Koch, S. Aloni, A. Schwartzberg, D. Ogletree, J. Neaton, and A. Weber-Bargioni, ACS Nano **13**, 10520 (2019).
[30] H. Qiu, T. Xu, Z. Wang, W. Ren, H. Nan, Z. Ni, Q. Chen, S. Yuan, F. Miao, F. Song, G. Long, Y. Shi, L. Sun, J. Wang, and X. Wang, Nat. Commun. **4**, 2642 (2013).
[31] J. A. A. Crossley, S. Myhra, and C. J. Sofield, Surf. Sci. **318**, 39 (1994).
[32] J. A. A. Crossley, C. J. Sofield, and S. Myhra, Surf. Sci. **380**, 568 (1997).
[33] H. Y. Song, and J. T. Lü, AIP Adv. **8**, 125323 (2018).
[34] M. Jana, A. Singh, A. Sampath, C. Rao, and U. Waghmare, Z. Anorg. Allg. Chem. **642**, 1386 (2016).
[35] L. Muechler, W. Hu, L. Lin, C. Yang, and R. Car, Phys. Rev. B **102**, 041103(R) (2020).
[36] K. Kawahara, Z. Ni, R. Arafune, T. Shirasawa, C. L. Lin, E. Minamitani, S. Watanabe, M. Kawai, and N. Takagi, Appl. Phys. Express **10**, 045702 (2017).
[37] G. Kresse and J. Furthmüller, Comput. Mater. Sci. **6**, 15 (1996).
[38] G. Kresse and J. Furthmöller, Phys. Rev. B **54**, 11169 (1996).
[39] P. E. Blöchl, Phys. Rev. B **50**, 17953 (1994).
[40] J. P. Perdew, K. Burke, and M. Ernzerhof, Phys. Rev. Lett. **77**, 3865 (1996).
[41] See Supplemental Material at http://link.aps.org/supplemental/10.1103/PhysRevB.106.075428 for more details on STM/STS results, simulated images, and additional oxygen exposure experiments.
[42] S. Haldar, H. Vovusha, M. K. Yadav, O. Eriksson, and B. Sanyal, Phys. Rev. B **92**, 235408 (2015).
[43] T. Y. Jeong, H. Kim, S.-J. Choi, K. Watanabe, T. Taniguchi, K. J. Yee, Y.-S. Kim, and S. Jung, Nat. Commun. **10**, 3825 (2019).
[44] C. J. Butler, P. Y. Yang, R. Sankar, Y. N. Lien, C. I. Lu, L. Y. Chang, C. H. Chen, C. M. Wei, F. C. Chou, and M. T. Lin, ACS Nano **10**, 9361 (2016).
[45] C. J. Butler, Y. M. Wu, C. R. Hsing, Y. Tseng, R. Sankar, C. M. Wei, F. C. Chou, and M. T. Lin, Phys. Rev. B **96**, 195125 (2017).
[46] S. Yuan, R. Roldán, M. I. Katsnelson, and F. Guinea, Phys. Rev. B **90**, 041402(R) (2014).